ARTICLE

High-Throughput and Self-Powered Electroporation System for Drug Delivery Assisted by Microfoam Electrode

Zhirong Liu, Xi Liang, Huanhuan Liu, Zhuo Wang, Tao Jiang, Yuanyuan Cheng, Mengqi Wu, Deli Xiang, Zhou Li, Zhong Lin Wang,* and Linlin Li*

Cite This: https://dx.doi.org/10.1021/acsnano.0c06100

Read Online

ACCESS | Metrics & More | Article Recommendations | SI Supporting Information

ABSTRACT: Electroporation is an effective approach for drug and gene delivery, but it is still limited by its low-throughput and severe cell damage. Herein, with a self-powered triboelectric nanogenerator as the power source, we demonstrated a high-throughput electroporation system based on the design of biocompatible and flexible polypyrrole microfoam as the electrode within the flow channel. In particular, to lower the imposed voltage, one-dimensional (1D) Ag nanowires were modified on the microfoam electrode to build up a locally enhanced electric field and reduce cell damage. The self-powered electroporation system realized a successful delivery of small and large biomolecules into different cell lines with efficiency up to 86% and cell viability over 88%. The handle throughput achieved as high as 10^5 cells min^{-1} on continuously flowed cells. The high-throughput and self-powered electroporation system is expected to have potential applications in the fields of high-throughput drug and gene delivery for *in vitro* isolated cells.

KEYWORDS: electroporation, microfoam electrode, high-throughput, self-powered, triboelectric nanogenerator, drug delivery
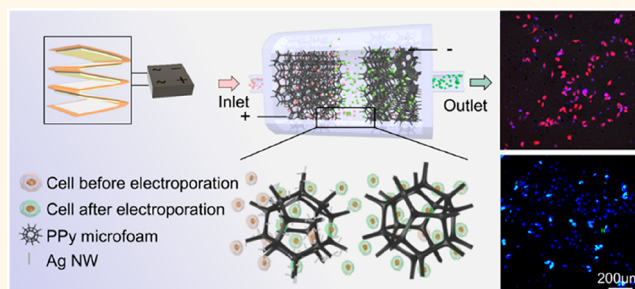
Nondestructive delivery of biologically active species into cells has a great significance for biotechnological research and therapeutic applications.[1−4] However, it is challenging because the selective permeability of the cell membrane prevents most biomolecules from accessing the cytosol.[5−7] Physical delivery methods (*e.g.*, microinjection,[8,9] electroporation,[10,11] and sonoporation[12−14]) primarily disrupt the cell membrane to increase membrane permeability for exogenous molecule delivery.[15−17] Among them, high-voltage electroporation can achieve fast intracellular delivery to various cell lines by optimization of the exerted electric field.[18−20] Nowadays, electroporation has been practically applied for monoclonal antibody production,[21] therapeutic DNA vaccination,[22] and T-cell-based immunotherapy.[23] However, the low cell throughput, high cell damage, and bulky size of the electroporation device have severely prohibited the broad applications of this technique.

To decrease the imposed voltage and reduce heat-induced cell damage, recent research advances have spawned 1D nanostructure-improved electroporation based on the "lightening rod effect".[24,25] The lightening rod effect happens when a conductive 1D structure is placed in a uniform electric field, and the electric field strength near the vicinity of tip can be greatly amplified.[26] Different from the conventional bulk electroporation with high electric field applied up to thousands of volts per centimeter, nanostructure-improved electroporation could enhance the localized electrical field intensity, thus reducing the imposed voltage and its accompanied damage to cells. 1D nanostructures, including nanostraws,[25] nanoneedles,[27] and nanowires,[26] have been introduced into the systems to realize a localized electroporation for intracellular drug delivery. More importantly, recent research, including ours, has successfully integrated a triboelectric nanogenerator (TENG)[28−32] into the systems, thus realizing self-powered electroporation without any additional power supply.[26,27,33] Due to its advantages of simple fabrication, cost-effectiveness, adjustable output, and availability of multifrequency resources,[34−39] the TENG has shown great potential in the
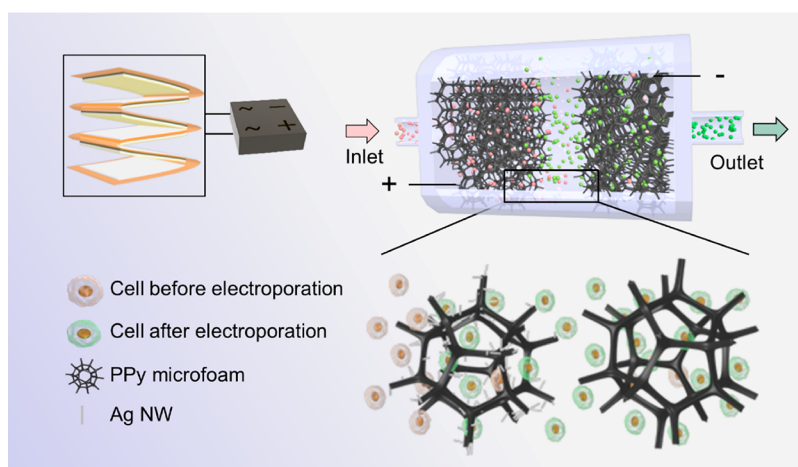
Figure 1. Schematic illustration of the TENG-driven high-throughput electroporation system.

biomedical field for both *in vivo* and *in vitro* applications.[40] However, for practical biomedical applications, a large number of cells need to be handled in one process to ensure consistent transfection. Nowadays, the existing high-throughput electroporation system typically has high cell damage,[41,42] relatively low-throughput,[17,43] or complicated operation.[42,44] Furthermore, most nanostructured electrodes[44] and microchannels[17,43] were fabricated by micromachining, which is time-consuming, prohibitive, and requires professional operation. Hence, it is still challenging to efficiently deliver active molecules into a large number of cells with low cell damage.

To solve these problems, herein, we proposed a high-throughput and self-powered electroporation system driven by a multilayered TENG, which could break through the limitation of traditional electroporation with low-throughput, low cell survival, and bulky device size. A biocompatible and flexible polypyrrole (PPy) microfoam electrode with a pore size of ~300 μm was fabricated to ensure the free passage of a cell suspension through the microchannels to achieve a high-throughput electroporation. To realize high transfection efficiency without sacrificing the cellular viability, 1D silver nanowires (Ag NWs) were modified on the PPy microfoam anode to build up a locally enhanced electric field. The pulsed voltage generated from the TENG as a power source provides a steady and direct current pulse for self-powered electroporation. When the cells pass through the Ag NW-modified PPy microfoam electrode, the continuously applied external electric field disrupts the cell membrane and drives exogenous molecules into the cytoplasm. This TENG-driven self-powered electroporation system could deliver different kinds of foreign species into various cell lines, including hard to transfect primary stem cells with a high-throughput of 10^5 cells min^{-1}. The delivery efficiency could reach 52−89% with a cell viability over 88%.

RESULTS AND DISCUSSION

Figure 1 illustrates the schematic diagram of the high-throughput electroporation device, which comprises three parts: a multilayered TENG as the source of electric pulses; a rectifier bridge that converts alternating current (AC) pulses into direct current (DC) pulses for electroporation; and (iii) a pair of microfoam electrodes placed in parallel within the flow channel. When the cell suspension driven by a syringe pump flows through the microfoam electrodes, the electric pulses

generated by the TENG are applied to the microfoam electrodes, which forms a pulsed electrical field between the cathode and the anode for cell electroporation. For the anode, PPy microfoam is modified with Ag NWs to generate a locally enhanced electric field for electroporation, thus reducing the external electric field and cell damage. The PPy microfoam as the cathode is not modified to reduce the cell mortality rate around the cathode.[45,46]

To ensure the cells with diameters of several to dozens of micrometers freely and continuously pass through the microfoam electrodes for high-throughput electroporation, 3D nickel (Ni) microfoam with a pore size of ~300 μm (2 × 4 cm, 2 mm thick) was chosen as the template on which to electrochemically grow PPy, whose pores were larger than the cells to ensure their flow through (Figure S1, Supporting Information). The fabrication process of the PPy microfoam is stepwisely illustrated in Figure 2a. In a three-electrode electrochemical workstation, the pyrrole monomers adsorbed on the Ni framework were polymerized into a PPy film, which forms a PPy@Ni core−shell microfoam (Figure S2, Supporting Information). To improve the biocompatibility of the electrode and prevent possible cytotoxicity caused by the precipitated nickel ions[47] or generated reactive oxygen species (ROS) under the applied voltage,[48] the Ni substrate was etched away with 1 M FeCl$_3$ solution to obtain a hollow PPy microfoam[49] (Figure 2b,c). The as-prepared PPy microfoam duplicated the continuous and interconnected 3D network structure of the Ni microfoam. The flexibility and hollow structure of PPy microfoam indicated the complete removal of the Ni template. In addition, it was flexible enough to be repeatedly bent without breaking (Figure 2b, inset), ensuring the prepared electrode was stable and durable for long electroporation times. The X-ray diffraction (XRD) result (Figure S3a, Supporting Information) shows that the broad peak diffraction at 25° is the characteristic peak of PPy. From the Fourier transform infrared (FT-IR) spectra (Figure S3b, Supporting Information), the peaks at 1527 cm^{-1} (Py ring vibration), 1452 cm^{-1} (=C−H in-plane vibration), 889 and 766 cm^{-1} (=C−H out-of-plane vibration), 1292 cm^{-1} (C−N stretching vibration), 1141 cm^{-1} (C−C stretching), and 1022 cm^{-1} (in-plane deformation of C−H and N−H bonds of the pyrrole ring) indicated that the microfoam consisted of PPy. Compared with the Ni microfoam, the surface of the PPy
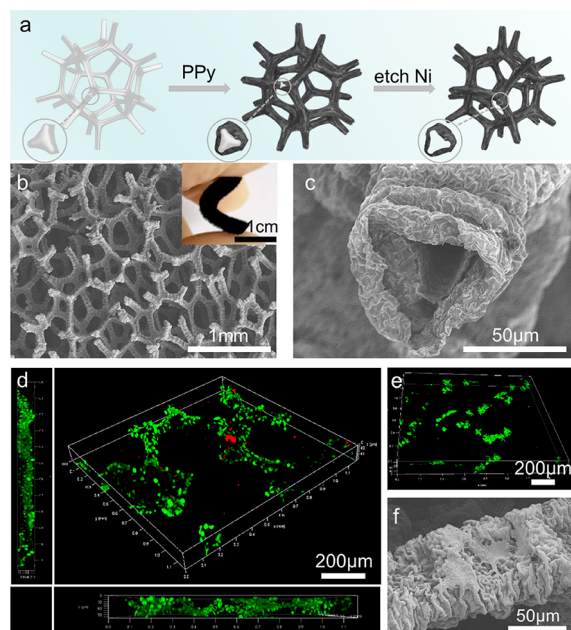
Figure 2. Fabrication and biocompatibility of the PPy microfoam. (a) Process diagram of PPy microfoam *via* the electrochemical deposition method. **(b,c)** SEM images of the PPy microfoam. **(d)** Cell viability assay of MCF-7 cells on the PPy microfoam after 48 h culture; live cells were stained with calcein AM (green), and dead cells were stained with propidium iodide (red) (scale bar = 200 μm). **(e)** 3D fluorescence microscopy images of MCF-7 cells on the PPy microfoam after 48 h culture. F-actin was stained with phalloidin−Alexa Fluor 488-labeled (green) (scale bar = 200 μm). **(f)** SEM image of MCF-7 cells on the PPy microfoam after 48 h culture (scale bar = 50 μm).

effect is still far from satisfactory. To avoid it, a low external voltage was applied and a locally enhanced electric field was built using 1D Ag NWs to modify the anode PPy microfoam, which would generate a local strong electric field near the Ag NWs, especially at the sharp nanoscaled tips (Figure 3a). The diameter of the Ag NWs was ∼50 nm, and the length ranged from 20 to 30 μm (Figure S9, Supporting Information). The high-resolution transmission electron microscopy (HRTEM) image (Figure 3b) shows that the spacing of the lattice planes was 0.235 nm, ascribed to the (111) plane of the face-centered cubic (fcc) silver crystal. The selected area electron diffraction (SAED) pattern (Figure 3c) shows there were two interpenetrated diffraction patterns: the square symmetry one (pink lines) originated from the [001] zone axis, and the other (blue line) corresponded to the [112] zone axis, indicating the twinned structure of the Ag NWs.[50−52] After the modification, the Ag NWs were evenly distributed on the framework of the PPy microfoam, and the structure of the microfoam had no obvious change (Figure 3a). The resistance of the PPy microfoam decreased from 650 to 120 Ω·cm after being modified with low-resistivity Ag NWs (∼0.006 Ω·cm). From the electrical field simulation in Figure 3d,e, the electric field at the tip of the Ag NWs could reach 9×10^5 V cm^{-1} under an imposed voltage of 20 V. In comparison, it was only 10 V cm^{-1} for the unmodified PPy microfoam electrode. Thus, the 9×10^4 times enhancement of the electric field intensity was generated at the tip of the Ag NWs (Figure 3d) compared with the unmodified PPy microfoam electrode (Figure 3e). After the 1D NWs were loaded, a lower external applied voltage would be adequate to generate a sufficiently high local electrical field for cell electroporation. Furthermore, as the electroporation occurred only within the limited area of the cell membrane near the Ag NWs, it could effectively avoid cell damage caused by heat generation in uniform high-voltage electroporation.

The multilayered TENG was employed due to its advantages of small size, light weight, and convenient driving, and its output voltage can be easily adjusted by changing the number of parallel units or the friction layer area. To meet the voltage required for electroporation, we prepared a multilayered TENG composed of five independent contact-separation mode TENG basic units (3 cm × 3 cm) in parallel, and a serrated Kapton strip (50 μm in thickness) served as the substrate. As shown in Figure 4a of the enlarged schematic diagram, each basic TENG unit was based on the contact and separation between the bottom copper (Cu) electrode and the upper polarized fluorinated ethylene propylene (FEP) film attached on another Cu electrode. To increase the stability and durability of the TENG, a 1 mm thick sponge layer was bound between the Kapton substrate and the Cu−FEP film as a stress buffer (Figure S10, Supporting Information). Figure 4b,c shows the working principle of the TENG basic unit. When the Cu and FEP film contact each other under pressing, the positive and negative triboelectric charges are generated on the bottom Cu and FEP surface, respectively. Upon releasing contact, an electric potential difference is induced between the two electrodes, which drives the free electron flow from the upper Cu to the bottom Cu electrode in the external circuit. The periodic press−release would produce an alternating current. The open-circuit voltage (V_{oc}) and transferred charge of the multilayered TENG driven by a mechanical linear motor under 2.5 Hz were 220 V and 780 nC, respectively (Figure 4d,e). The TENG had an outstanding durability, and the V_{oc}

microfoam was rougher, which was beneficial to the attachment of the Ag NWs.
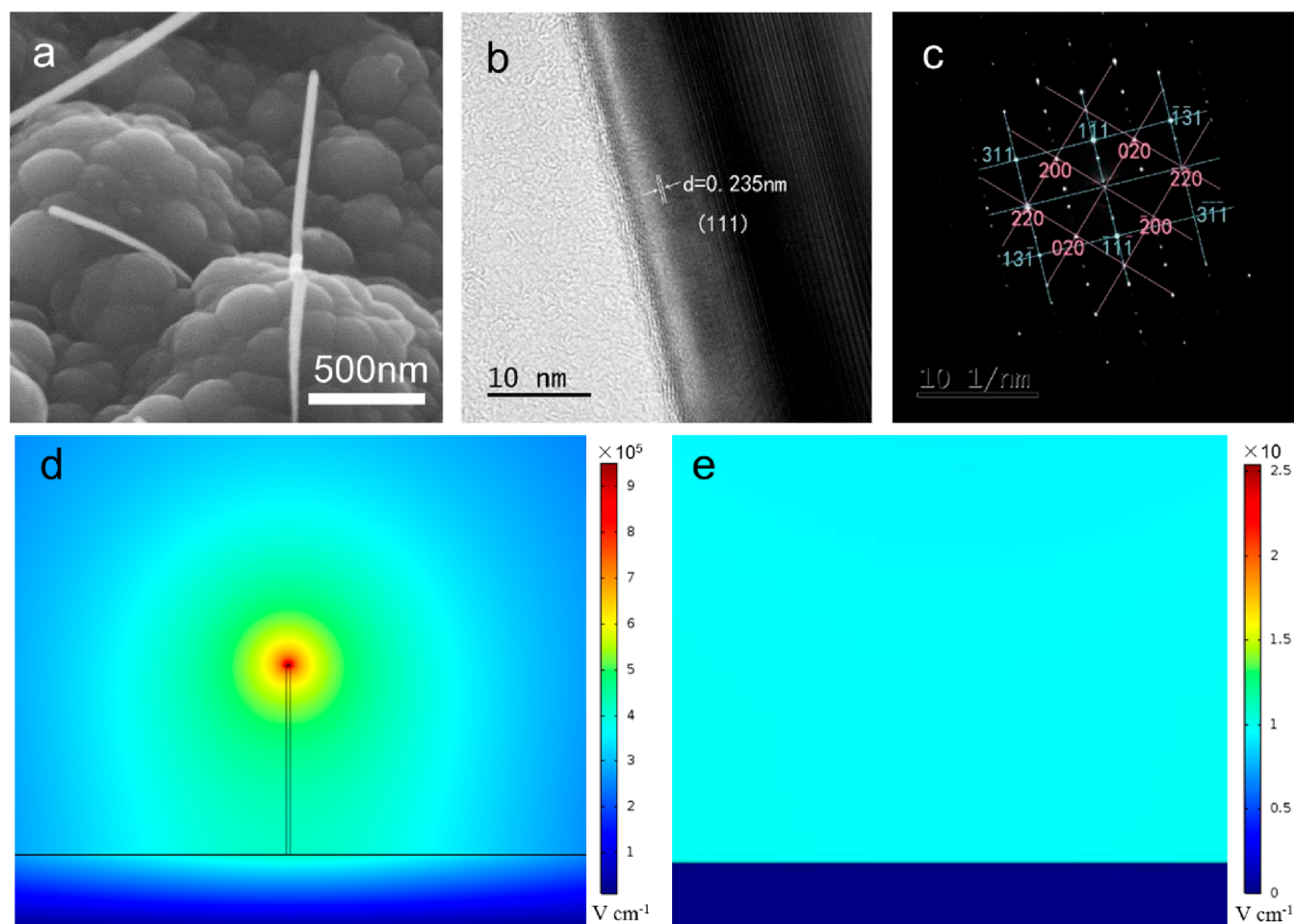
MCF-7 breast cancer cells and rat bone mesenchymal stem cells (rBMSCs) were used as the model cells to study the biocompatibility of the PPy microfoam *via* a live/dead cell staining assay, where live cells were stained with green (calcein AM) and dead cells with red (propidium iodide, PI). After being cultured on the PPy substrate for 48 h, ∼93.7% of MCF-7 cells and ∼95.2% of rBMSCs were still alive, indicating that the PPy microfoam did not have an adverse effect on the cells (Figure 2d and Figures S4 and S5, Supporting Information). To further confirm the biocompatibility of the PPy microfoam, the cytoskeleton of the cells after being cultured for 48 h was stained with phalloidin−Alexa Fluor 488, and the cell nuclei were stained with 4′,6-diamidino-2-phenylindole (DAPI) (Figure 2e and Figures S6 and S7, Supporting Information). The distribution of the cells was consistent with the skeleton structure of the microfoam, indicating that the cells could attach and survive well on the framework of the PPy microfoam. The morphologies of the cells cultured on the PPy microfoam were also observed *via* scanning electron microscopy (SEM). The cells on the PPy microfoam displayed a natural spreading state compared to the control cells grown on the tissue culture plate (Figure 2f and Figure S8, Supporting Information), suggesting that the PPy microfoam was biocompatible, and it would not disrupt the growth and attachment of the cells.

In traditional electroporation, its uniform high voltage and strong electric field induce low cell viability. Strict temperature control is often needed to reduce thermal damage, but the

Figure 3. Ag NW-modified PPy microfoam enhanced the localized electrical field. (a) SEM image of the Ag NW-modified PPy microfoam. (b) HRTEM image and (c) SAED pattern of the Ag NW. The simulated electrical field distribution of the (d) Ag NW-modified PPy microfoam and (e) PPy microfoam at an imposed voltage of 20 V.

maintained high stability after 10000 cycles (Figure 4d). Further investigation of the power-resistance relationship of the multilayered TENG showed that the instantaneous voltage increased with the increase of the load resistances (Figure 4f). The instantaneous output power of the TENG reached the peak of 20 mW under the 1 MΩ matched resistance. A rectifier bridge was employed to transform the alternating current pulses into direct current pulses. Because the internal resistance of the TENG is relatively large, its open-circuit voltage is higher than the voltage on the application circuit of electroporation, and the output voltage of the TENG transferred to the electroporation system was ∼20 V, as measured by a digital oscilloscope (Figure 4g).

We verified the feasibility of the self-powered system for cell electroporation. Two parallel microfoam electrodes were immobilized in the 24-well plate with a distance of 2 mm. We first investigated the effect of voltage magnitude on the electroporation to deliver fluorescein isothiocyanate (FITC)-labeled dextran (FITC-dextran, 10 kDa) into MCF-7 cells (Figure S11, Supporting Information). At the fixed frequency of 5 Hz, pulse number of 200, and pulse width of 500 μs, the cell viability gradually decreased from 92% (at 10 V) to 74% (at 80 V) when the voltage increased. However, the delivery efficiency at 10 V was only 51.0 ± 5.9%. In contrast, the delivery efficiency at 20 V was 83.7 ± 3.1% with a high cell viability of 84.3%. We also investigated the effect of electrical

stimulation frequency and pulse numbers on the delivery efficiency and cell viability. At the fixed pulse number of 200, the delivery efficiency gradually increased from 21% (at 2 Hz) to 86% (at 8 Hz) when the electrical stimulation frequency increased. However, for electrical stimulation with 8 Hz, the TENG was driven by a linear motor (4 Hz) to generate continuous electrical pulses because it is difficult to achieve such a high frequency with human hand-slapping. In addition, when the other parameters were the same, extension of the electrical stimulation time could improve the drug delivery efficiency from 84% (200 pulses) to 90% (400 pulses) for 20 V. However, the cell viability was significantly reduced from 86 to 72%. The delivery efficiency and cell viability after electroporation with different electrodes (whether or not modified with Ag NWs) were also performed, and group +/− (anode: Ag NWs modified PPy microfoam; cathode: PPy microfoam) showed the optimal delivery efficiency without obviously sacrificing cell viability (Figure S13, Supporting Information). Therefore, with comprehensive consideration of delivery efficiency, cell viability, and convenience of operation, we chose the electroporation parameters of 20 V, 5 Hz, and 200 pulses in the following work, and Ag NWs were only modified on the PPy microfoam anode.

A membrane-impermeable molecule PI (weight = 668.39 Da) was used as the model drug to observe its delivery efficiency into MCF-7 cells. Electrical pulses were applied onto
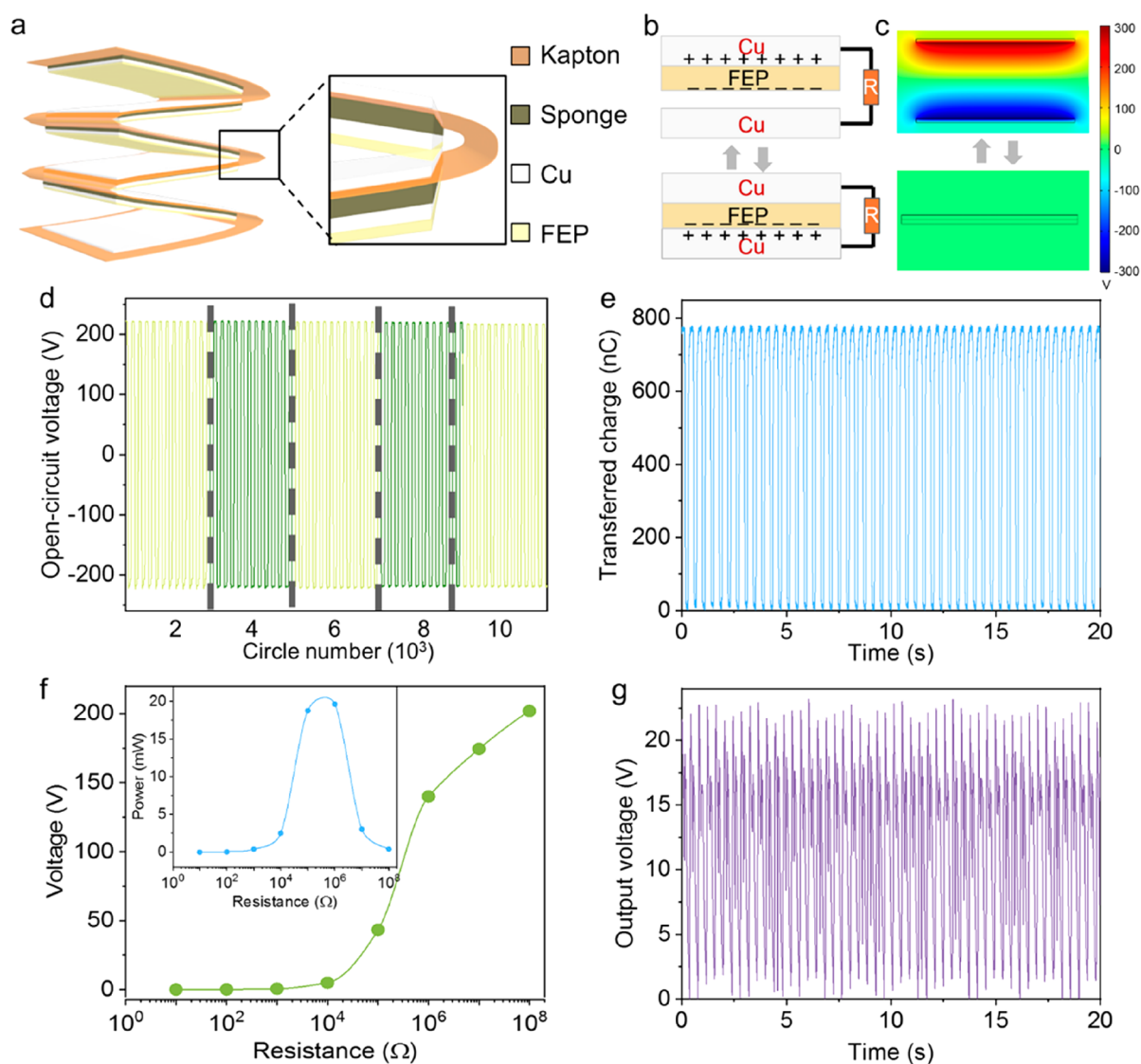
Figure 4. Structure and output performance of the multilayered TENG. (a) Schematic diagram of the multilayered TENG and local enlarged structure of the basic unit. (b) Working principle and (c) COMSOL simulation of each TENG unit of the multilayered TENG. (d) Open-circuit voltage and (e) transferred charge of the multilayered TENG driven by a linear motor under 2.5 Hz. (f) Voltage and peak power density at different load resistances. (g) Voltage transferred to the electroporation system after rectification.

the electrodes by the multilayered TENG with periodic hand-slapping (2.5 Hz, 40 s), and a control group test was performed under identical conditions without electric stimulation of the TENG. The fluorescent images showed that the TENG-enabled electroporation realized an 89.4% PI delivery (red fluorescence in Figure 5a) into MCF-7 cells, significantly higher than that of the control group without electroporation (6.9%) and that with flat electrode and TENG-enabled electroporation (<3%) (Figure S14a,b, Supporting Information). In addition, antitumoral doxorubicin hydrochloride (DOX) as a functional biomolecule was also employed to further improve intracellular delivery for both MCF-7 breast cancer cells and corresponding DOX drug-resistant MCF-7/ADR. From Figure S15 in the Supporting Information, DOX successfully entered most cells after electroporation, with a delivery efficiency of 94.2% for MCF-7 and 65.3% for MCF-7/ADR. At 24 h post-electroporation, the cell viability was 31.0% for MCF-7 and 55.1% for MCF-7/ADR. In comparison, a 24 h treatment of MCF-7/ADR with DOX (without electro-

poration) had only a ~10% cell killing percentage in our previous results.[6] These results show the advantages of an electroporation system for drug delivery, with a very short drug action time. For macrobiomolecules, delivery into cells is rather difficult due to the large molecular weight and low diffusion rate. Our self-powered electroporation system successfully delivered macromolecular FITC-dextran (10 kDa) into MCF-7 cells with a high efficiency of 89.5% (Figure 5b,d). After 24 h of electroporation, the cell viability was still higher than 77% (Figure 5e). These results demonstrated the advantages of the system with high delivery efficiency and minimal cellular disruption.

Intracellular delivery into hard to transfect primary cells has always been challenging. To demonstrate our system's potential as a promising universal alternative for cytosolic delivery, we tested the delivery efficiency in hard to transfect rBMSCs. The delivery efficiency of FITC-dextran was up to 66.1%, and the cell viability was higher than 85% (Figure 5c−e). These results demonstrated that our self-powered TENG-
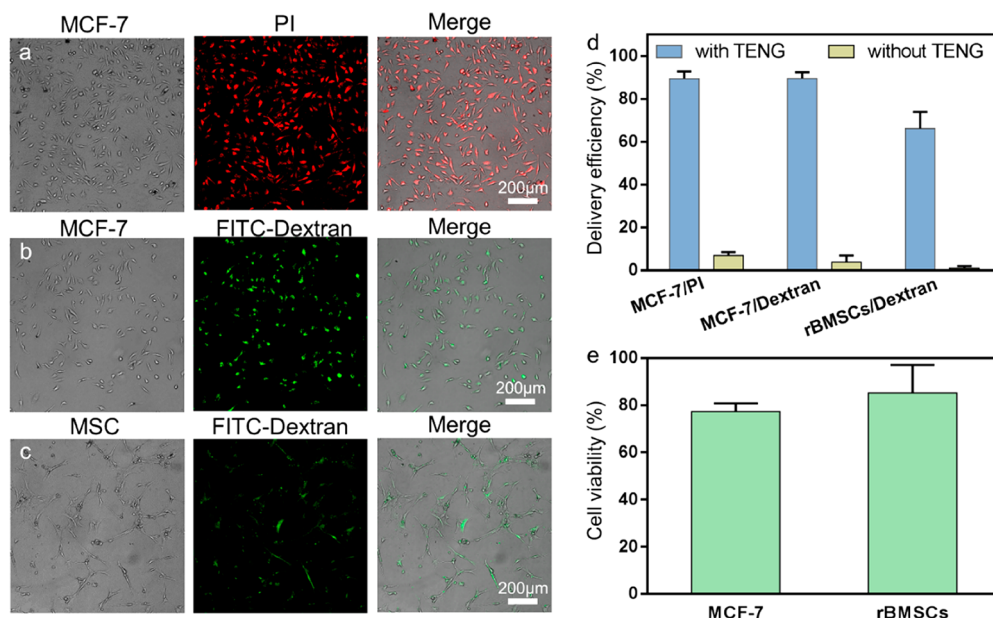
Figure 5. Delivery of biomolecular species into multiple cell types. (a) PI delivery into MCF-7 cells. Successfully delivered cells are red. FITC-dextran delivery into (b) MCF-7 cells and (c) rBMSCs. Successfully delivered cells were green (scale bar = 200 μm). (d) Quantitative delivery efficiency of MCF-7 cells and rBMSCs. (e) Cell viability of MCF-7 cells and rBMSCs after electroporation.
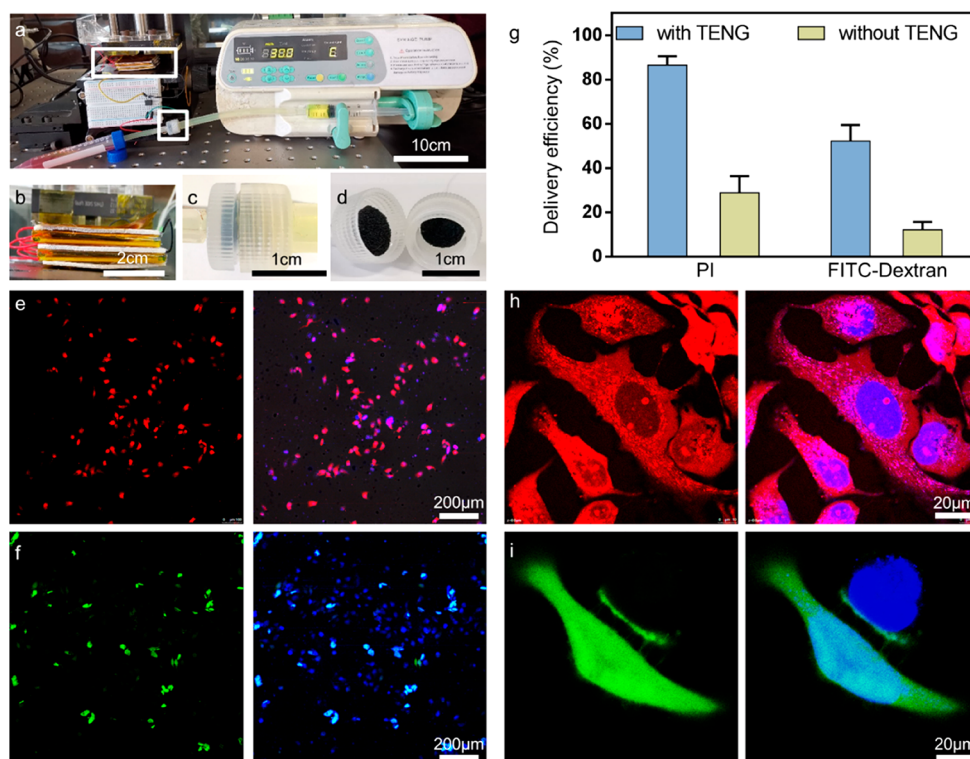
Figure 6. High-throughput intracellular delivery of diverse biological species. (a) Photograph of the high-throughput electroporation system. Photograph of the (b) multilayered TENG and (c,d) pair of PPy microfoam electrodes in the filter shell. (e,h) High-throughput PI delivery into MCF-7 cells. Successfully delivered cells were red. (f,i) High-throughput FITC-dextran delivery into MCF-7 cells. Successfully delivered cells were green. (g) Quantitative delivery efficiency of MCF-7 cells.

driven electroporation system could efficiently deliver a broad range of exogenous materials into multiple cell types with minor damage to cells.

After proving the high delivery efficiency and low cell damage of the self-powered electroporation system, we set up a high-throughput electroporation system (Figure 6a). Because the high-throughput electroporation required long-term electrical stimulation onto continuously flowed cells, the multilayered TENG was driven by a linear motor (7 N, 2.5 Hz) to generate continuous electrical pulses (Figure 6b), and a rectifier bridge was employed to convert AC pulses into DC pulses. A pair of microfoam electrodes were placed in parallel

within the flow channel (in a filter shell): the Ag NW-modified PPy microfoam was connected to the positive output terminal of the rectifier bridge as the anode, and the PPy microfoam without Ag NWs was connected to the negative output terminal of the rectifier bridge as the cathode (Figure 6c,d). Thus, there was a pulsed electrical field between the cathode and the anode when the electric pulses generated by the TENG were imposed. According to Figure 2b, the pore size of the PPy microfoam was ~300 μm, which was much larger than the cells. So, the cells could smoothly pass through the electroporation flow channel, and the cells' post-electroporation could be collected into a collection tube. The MCF-7 cells suspended in the electroporation buffer (2×10^5 cells mL^{-1}) were passed through the high-throughput electroporation system at a flow rate of 30 mL h^{-1} driven by a syringe pump. When the cells were located between the two foam electrodes, the permeability of the cellular membrane increased under the strong electric field, and the foreign molecules could diffuse into the cells. The delivery efficiency of PI and FITC-dextran was 86 and 52%, respectively (Figure 6e−g). In comparison, it was only 29% for PI and 12% for FITC-dextran when the cell flowed through the microfoam electrodes but without TENG electric pulses (Figure S17, Supporting Information). The cell viability of the MCF-7 cells after the electroporation was higher than 88%, indicating that most cells passed through the PPy microfoam electrodes without cell damage. From the fluorescence images of the cells after delivery, some cells displayed a uniform cytosolic distribution of red and green fluorescence (Figure 6h,i), implying that the PI and FITC-dextran were likely to be directly delivered into the cytosol.[53]

High-throughput delivery of biological species into cells is a prerequisite for biological and medical applications. The most common method to increase the throughput is to execute electroporation in a multiwell plate by modifying the array electrodes in the well,[42,44,54−56] which could increase cell processing capacity to some extent, but it is too cumbersome for high-throughput delivery. A convenient way for high-throughput delivery is to allow the cell suspension parallel flows through the electrodes, which can achieve a high-throughput of 2×10^7 min^{-1}, but the viability of the cells after electroporation was only 50−60%.[41] Recent research has designed microfluidic devices to create rapid mechanical deformation in cell membranes, followed by electroporation.[17,43,57] This system has high delivery efficiency with low cell damage, but due to the single-cell treatment, multiple parallel channels are required to increase throughput. By contrast, our self-powered electroporation system achieves a cell throughput of 10^5 cells min^{-1} with high delivery efficiency of 86% and cell viability over 88%, proving the advantages of the TENG-driven electroporation system for high-throughput intracellular delivery. Furthermore, the self-powered system that could be operated by a biomechanical energy-driven TENG would realize energy economy and emergency applications.

CONCLUSIONS

Our self-powered electroporation system is able to deliver a variety of molecules into the cytoplasm of multiple cell types with high-throughput, high delivery efficiency, and minimal cell damage. The 1D Ag NW-modified PPy microfoam as the electrode decreases the imposed voltage and allows the cell suspension to freely pass through the system to achieve a high-throughput electroporation. The locally enhanced electrical field in the limited area near the tip of the nanowires decreased the imposed voltage and caused minimal cell damage. The TENG as an emerging energy technology was employed to transfer biomechanical energy to electric pulses for self-powered electroporation. Due to its advantages of adjustable output, cost-effectiveness, and excellent durability, the integrated electroporation device is lightweight and portable. We anticipate that such a high-throughput and self-powered intracellular delivery will have great potential in fundamental biology and medical applications.

EXPERIMENTAL SECTION

Fabrication of the Multilayered TENG. A 50 μm thick Kapton strip (24 cm × 4 cm) was folded evenly into six squares (4 cm × 4 cm), forming a serrated structure that served as the substrate of the TENG. Then, a Cu foil and a Cu−FEP film (3 cm × 3 cm) were adhered on the two opposite surfaces of the Kapton strip, and a 1 mm thick sponge layer (3.2 cm × 3.2 cm) was attached between the Kapton strip and the Cu−FEP film to ensure an intimate contact between two triboelectric materials (the Cu foil and the FEP film). Electrons were injected to the FEP layer surfaces to increase the surface charges at a polarization voltage of 5 kV for 5 min. The electric outputs of the multilayered TENG were measured with an electrometer (Keithley 6514). The alternating current pulses generated by the TENG were transformed to direct current pulses through a rectifier bridge, and the output performance was measured with a digital oscilloscope (Agilent InfiniiVision 2000X).

Synthesis of 3D PPy Microfoam. The Ni microfoam (4 cm × 2 cm × 0.2 cm) was ultrasonically cleaned in 1 M HCl, ethanol, and deionized water for 10 min. Pyrrole (Py, Aladdin) monomer (5 mL) was added into 0.3 M NaClO$_4$ solution (100 mL) and stirred for 10 min. The electropolymerization of Py was carried out in a three-electrode electrochemical workstation (CHI 660F Instruments). The Ni microfoam, Pt, and Ag/AgCl were used as the working, counter, and reference electrodes, respectively. The electropolymerization process was performed in the Py/NaClO$_4$ solution under the potential of 0.8 V for 300−500 s. Subsequently, the fabricated PPy@Ni microfoam was immersed in 1 M FeCl$_3$ solution for 6−8 h to etch the Ni microfoam and to obtain the 3D PPy microfoam.

Synthesis of Ag NW/PPy Microfoam. The Ag NWs (Nanjing XFNANO Materials Tech Co., Ltd.) was dispersed in water at the concentration of 1 mg mL^{-1} and dispersed by ultrasound for 15 min. The as-prepared PPy microfoam was dipped in the Ag NW ink, oscillated with a shaking table for 30 min, and dried at 60 °C. Then, the samples were washed with deionized water to obtain Ag NW/Ppy microfoam. The surface morphology of the samples was characterized by SEM (SU8020, Hitachi). The TEM images of the Ag NWs were acquired on a FEI/Tecnai G2 F20 S-TWIN TMP microscope with an operating voltage of 200 kV. XRD pattern was obtained with a Bruker D8 Advance powder X-ray diffractometer with Cu Kα radiation (λ = 0.15406 nm). The FT-IR spectrum was obtained with Bruker VERTEX 80v. Micro-computed tomography imaging was acquired with a Quantum GX (PerkinElmer).

Electroporation. The 1 × 1 cm Ag NW/PPy microfoam and PPy microfoam were pasted on the bottom and the cap of a 24-well plate as the anode and the cathode, respectively. The distance between the two microfoams was 2 mm. Before electroporation, the electrodes were sterilized with 70% ethanol and UV exposure and rinsed three times with sterilized water. Then, the cells were collected, rinsed three times with Dulbecco's phoshate-buffered saline (DPBS), and resuspended in DPBS with 100 μg mL^{-1} PI or 200 μg mL^{-1} FITC-dextran or 100 μM DOX (1 × 10^6 cells mL^{-1}). Electrical pulses were applied by the multilayered TENG (2.5 Hz, 40 s) with periodic hand-slapping. To estimate whether the electric potential difference generated by the TENG was transferred to the electroporation system, and the voltage between the two microfoam electrodes was measured with a digital oscilloscope. After electroporation, 0.5 mL

growth medium was added to the 24-well plate and incubated at 37 °C for 15 min to allow exogenous molecules to enter the cells. Then, the cells were collected, centrifuged, suspended in the growth medium, and transferred to a glass Petri dish for further observation. For comparison, cells incubated in the PPy microfoam electrode without electrical pulses were also observed.

High-Throughput Electroporation. A 10 mL cell suspension (5 × 10⁵ cells mL⁻¹, in electroporation buffer) was passed through the PPy microfoam filter at a flow rate of 30 mL h⁻¹. At the same time, electrical pulses were applied by the multilayered TENG (2.5 Hz) driven by a linear motor. The cell suspension after electroporation was collected in a 15 mL centrifuge tube with 5 mL of culture medium. Then, the cell suspension was incubated at 37 °C for 15 min, suspended in the growth medium, stained with DAPI for the nuclei, and observed after cell adhesion.

Cell Viability Assay. To assess the viability of the cells after electroporation, the cells were cultured on a 48-well plate for another 24 h, and the viability of the cells was quantitatively evaluated with a cell count kit-8 (CCK-8, Dojindo Molecular Technology) according to the manufacturer's instructions. Three parallel replicates for each group were used.

Statistical Analysis. The data are reported as the means ± standard deviation, and statistical analysis was performed using the unpaired Student's t test.

ASSOCIATED CONTENT

Ⓢ Supporting Information

The Supporting Information is available free of charge at https://pubs.acs.org/doi/10.1021/acsnano.0c06100.

> Cell culture, biocompatibility evaluation of the PPy microfoam, immunofluorescence staining, SEM observation of the cells, SEM images of PPy and Ni microfoam with different pore sizes, XRD and FT-IR spectra, cell viability evaluation of MCF-7 and rBMSCs, SEM and TEM images of the Ag NWs, photographs of the multilayered TENG, cell viability and delivery efficiency after electroporation under different conditions, high-throughput PI delivery under different conditions, and the delivery efficiency and cell viability by a commercial electroporation system (PDF)

AUTHOR INFORMATION

Corresponding Authors

Linlin Li − *Chinese Academy of Sciences (CAS) Center for Excellence in Nanoscience, Beijing Institute of Nanoenergy and Nanosystems, Chinese Academy of Sciences, Beijing 100083, P.R. China; School of Nanoscience and Technology, University of Chinese Academy of Sciences, Beijing 100049, P.R. China;* ⓞ orcid.org/0000-0003-1041-4533; Email: lilinlin@binn.cas.cn

Zhong Lin Wang − *Chinese Academy of Sciences (CAS) Center for Excellence in Nanoscience, Beijing Institute of Nanoenergy and Nanosystems, Chinese Academy of Sciences, Beijing 100083, P.R. China; School of Nanoscience and Technology, University of Chinese Academy of Sciences, Beijing 100049, P.R. China; School of Materials Science and Engineering, Georgia Institute of Technology, Atlanta, Georgia 30332-0245, United States;* Email: zhong.wang@mse.gatech.edu

Authors

Zhirong Liu − *Chinese Academy of Sciences (CAS) Center for Excellence in Nanoscience, Beijing Institute of Nanoenergy and Nanosystems, Chinese Academy of Sciences, Beijing 100083, P.R. China; School of Nanoscience and Technology, University of Chinese Academy of Sciences, Beijing 100049, P.R. China*

Xi Liang − *Chinese Academy of Sciences (CAS) Center for Excellence in Nanoscience, Beijing Institute of Nanoenergy and Nanosystems, Chinese Academy of Sciences, Beijing 100083, P.R. China; School of Nanoscience and Technology, University of Chinese Academy of Sciences, Beijing 100049, P.R. China*

Huanhuan Liu − *Chinese Academy of Sciences (CAS) Center for Excellence in Nanoscience, Beijing Institute of Nanoenergy and Nanosystems, Chinese Academy of Sciences, Beijing 100083, P.R. China; Department of Biological Sciences, School of Life Science, Anhui University, Hefei 230601, P.R. China*

Zhuo Wang − *Chinese Academy of Sciences (CAS) Center for Excellence in Nanoscience, Beijing Institute of Nanoenergy and Nanosystems, Chinese Academy of Sciences, Beijing 100083, P.R. China; School of Nanoscience and Technology, University of Chinese Academy of Sciences, Beijing 100049, P.R. China*

Tao Jiang − *Chinese Academy of Sciences (CAS) Center for Excellence in Nanoscience, Beijing Institute of Nanoenergy and Nanosystems, Chinese Academy of Sciences, Beijing 100083, P.R. China; School of Nanoscience and Technology, University of Chinese Academy of Sciences, Beijing 100049, P.R. China*

Yuanyuan Cheng − *Department of Biological Sciences, School of Life Science, Anhui University, Hefei 230601, P.R. China*

Mengqi Wu − *Chinese Academy of Sciences (CAS) Center for Excellence in Nanoscience, Beijing Institute of Nanoenergy and Nanosystems, Chinese Academy of Sciences, Beijing 100083, P.R. China; School of Nanoscience and Technology, University of Chinese Academy of Sciences, Beijing 100049, P.R. China*

Deli Xiang − *Chinese Academy of Sciences (CAS) Center for Excellence in Nanoscience, Beijing Institute of Nanoenergy and Nanosystems, Chinese Academy of Sciences, Beijing 100083, P.R. China*

Zhou Li − *Chinese Academy of Sciences (CAS) Center for Excellence in Nanoscience, Beijing Institute of Nanoenergy and Nanosystems, Chinese Academy of Sciences, Beijing 100083, P.R. China; School of Nanoscience and Technology, University of Chinese Academy of Sciences, Beijing 100049, P.R. China;* ⓞ orcid.org/0000-0002-9952-7296

Complete contact information is available at:
https://pubs.acs.org/10.1021/acsnano.0c06100

Author Contributions

L.L.L., Z.L.W., and Z.R.L. conceived the project. Z.R.L. and H.H.L. designed and conducted the cell electroporation. X.L. and T.J. designed the TENG. Z.W., Y.Y.C., M.Q.W., D.L.X., and Z.L. produced data analysis plots. Z.R.L., L.L.L., and Z.L.W. revised the paper. All co-authors reviewed and edited the paper. Z.R.L. and X.L. contributed equally to this work.

Notes

The authors declare no competing financial interest.

REFERENCES

(1) Kim, Y. B.; Zhao, K. T.; Thompson, D. B.; Liu, D. R. An Anionic Human Protein Mediates Cationic Liposome Delivery of Genome Editing Proteins into Mammalian Cells. *Nat. Commun.* **2019**, *10*, 2905.

(2) Mura, S.; Nicolas, J.; Couvreur, P. Stimuli-Responsive Nano-carriers for Drug Delivery. *Nat. Mater.* **2013**, *12*, 991−1003.

(3) Tang, F. Q.; Li, L. L.; Chen, D. Mesoporous Silica Nanoparticles: Synthesis, Biocompatibility and Drug Delivery. *Adv. Mater.* **2012**, *24*, 1504−1534.

(4) Langer, R. Drug Delivery and Targeting. *Nature* **1998**, *392*, 5−10.

(5) Whitehead, K. A.; Langer, R.; Anderson, D. G. Knocking Down Barriers: Advances in siRNA Delivery. *Nat. Rev. Drug Discovery* **2009**, *8*, 129−138.

(6) Wang, S.; Liu, X.; Chen, S. Z.; Liu, Z. R.; Zhang, X. D.; Liang, X.-J.; Li, L. L. Regulation of Ca2+ Signaling for Drug-Resistant Breast Cancer Therapy with Mesoporous Silica Nanocapsule Encapsulated Doxorubicin/siRNA Cocktail. *ACS Nano* **2019**, *13*, 274−283.

(7) Nakamura, T.; Yamada, Y.; Sato, Y.; Khalil, I. A.; Harashima, H. Innovative Nanotechnologies for Enhancing Nucleic Acids/Gene Therapy: Controlling Intracellular Trafficking to Targeted Biodistribution. *Biomaterials* **2019**, *218*, 119329.

(8) Adamo, A.; Jensen, K. F. Microfluidic Based Single Cell Microinjection. *Lab Chip* **2008**, *8*, 1258−1261.

(9) Tiefenboeck, P.; Kim, J. A.; Leroux, J. C. Intracellular Delivery of Colloids: Past and Future Contributions from Microinjection. *Adv. Drug Delivery Rev.* **2018**, *132*, 3−15.

(10) Kim, K.; Lee, W. G. Electroporation for Nanomedicine: A Review. *J. Mater. Chem. B* **2017**, *5*, 2726−2738.

(11) Hur, J. K.; Kim, K.; Been, K. W.; Baek, G.; Ye, S.; Hur, J. W.; Ryu, S. M.; Lee, Y. S.; Kim, J. S. Targeted Mutagenesis in Mice by Electroporation of Cpf1 Ribonucleoproteins. *Nat. Biotechnol.* **2016**, *34*, 807−808.

(12) Marmottant, P.; Hilgenfeldt, S. Controlled Vesicle Deformation and Lysis by Single Oscillating Bubbles. *Nature* **2003**, *423*, 153−156.

(13) van Wamel, A.; Kooiman, K.; Harteveld, M.; Emmer, M.; ten Cate, F. J.; Versluis, M.; de Jong, N. Vibrating Microbubbles Poking Individual Cells: Drug Transfer into Cells *via* Sonoporation. *J. Controlled Release* **2006**, *112*, 149−155.

(14) Bez, M.; Foiret, J.; Shapiro, G.; Pelled, G.; Ferrara, K. W.; Gazit, D. Nonviral Ultrasound-Mediated Gene Delivery in Small and Large Animal Models. *Nat. Protoc.* **2019**, *14*, 1015−1026.

(15) Meacham, J. M.; Durvasula, K.; Degertekin, F. L.; Fedorov, A. G. Physical Methods for Intracellular Delivery: Practical Aspects from Laboratory Use to Industrial-Scale Processing. *Jala* **2014**, *19*, 1−18.

(16) Wells, D. J. Gene Therapy Progress and Prospects: Electroporation and Other Physical Methods. *Gene Ther.* **2004**, *11*, 1363−1369.

(17) Ding, X. Y.; Stewart, M. P.; Sharei, A.; Weaver, J. C.; Langer, R. S.; Jensen, K. F. High-Throughput Nuclear Delivery and Rapid Expression of DNA *via* Mechanical and Electrical Cell-Membrane Disruption. *Nat. Biomed. Eng.* **2017**, *1*, 0039.

(18) Alvarez-Erviti, L.; Seow, Y. Q.; Yin, H. F.; Betts, C.; Lakhal, S.; Wood, M. J. A. Delivery of siRNA to the Mouse Brain by Systemic Injection of Targeted Exosomes. *Nat. Biotechnol.* **2011**, *29*, 341−345.

(19) Widera, G.; Austin, M.; Rabussay, D.; Goldbeck, C.; Barnett, S. W.; Chen, M. C.; Leung, L.; Otten, G. R.; Thudium, K.; Selby, M. J.; Ulmer, J. B. Increased DNA Vaccine Delivery and Immunogenicity by Electroporation *in Vivo*. *J. Immunol.* **2000**, *164*, 4635−4640.

(20) Dower, W. J.; Miller, J. F.; Ragsdale, C. W. High-Efficiency Transformation of Escherichia-Coli by High-Voltage Electroporation. *Nucleic Acids Res.* **1988**, *16*, 6127−6145.

(21) Tjelle, T. E.; Corthay, A.; Lunde, E.; Sandlie, I.; Michaelsen, T. E; Mathiesen, I.; Bogen, B. Monoclonal Antibodies Produced by Muscle after Plasmid Injection and Electroporation. *Mol. Ther.* **2004**, *9*, 328−336.

(22) Bodles-Brakhop, A. M.; Heller, R.; Draghia-Akli, R. Electroporation for the Delivery of DNA-Based Vaccines and Immunotherapeutics: Current Clinical Developments. *Mol. Ther.* **2009**, *17*, 585−592.

(23) Klebanoff, C. A.; Rosenberg, S. A.; Restifo, N. P. Prospects for Gene-Engineered T Cell Immunotherapy for Solid Cancers. *Nat. Med.* **2016**, *22*, 26−36.

(24) Liu, C.; Xie, X.; Zhao, W. T.; Liu, N.; Maraccini, P. A.; Sassoubre, L. M.; Boehm, A. B.; Cui, Y. Conducting Nanosponge Electroporation for Affordable and High-Efficiency Disinfection of Bacteria and Viruses in Water. *Nano Lett.* **2013**, *13*, 4288−4293.

(25) Xie, X.; Xu, A. M.; Leal-Ortiz, S.; Cao, Y. H.; Garner, C. C.; Melosh, N. A Nanostraw-Electroporation System for Highly Efficient Intracellular Delivery and Transfection. *ACS Nano* **2013**, *7*, 4351−4358.

(26) Yang, C. B.; Yang, G.; Ouyang, Q. L.; Kuang, S. Y.; Song, P. Y.; Xu, G. X.; Poenar, D. P.; Zhu, G.; Yong, K. T.; Wang, Z. L. Nanowire-Array-Based Gene Electro-Transfection System Driven by Human-Motion Operated Triboelectric Nanogenerator. *Nano Energy* **2019**, *64*, 103901.

(27) Liu, Z.; Nie, J.; Miao, B.; Li, J.; Cui, Y.; Wang, S.; Zhang, X.; Zhao, G.; Deng, Y.; Wu, Y.; Li, Z.; Li, L.; Wang, Z. L. Self-Powered Intracellular Drug Delivery by a Biomechanical Energy-Driven Triboelectric Nanogenerator. *Adv. Mater.* **2019**, *31*, 1807795.

(28) Liang, X.; Jiang, T.; Liu, G.; Xiao, T.; Xu, L.; Li, W.; Xi, F.; Zhang, C.; Wang, Z. L. Triboelectric Nanogenerator Networks Integrated with Power Management Module for Water Wave Energy Harvesting. *Adv. Funct. Mater.* **2019**, *29*, 1807241.

(29) Wang, Z. L. Entropy Theory of Distributed Energy for Internet of Things. *Nano Energy* **2019**, *58*, 669−672.

(30) Wu, C. S.; Wang, A. C.; Ding, W. B.; Guo, H. Y.; Wang, Z. L. Triboelectric Nanogenerator: A Foundation of the Energy for the New Era. *Adv. Energy Mater.* **2019**, *9*, 1802906.

(31) Fan, F. R.; Tian, Z. Q.; Wang, Z. L. Flexible Triboelectric Generator! *Nano Energy* **2012**, *1*, 328−334.

(32) Wang, Z. L.; Wang, A. C. On the Origin of Contact-Electrification. *Mater. Today* **2019**, *30*, 34−51.

(33) Wu, C. S.; Jiang, P.; Li, W.; Guo, H. Y.; Wang, J.; Chen, J.; Prausnitz, M. R.; Wang, Z. L. Self-Powered Iontophoretic Transdermal Drug Delivery System Driven and Regulated by Biomechanical Motions. *Adv. Funct. Mater.* **2020**, *30*, 1907378.

(34) Zhao, G. R.; Zhang, Y. M.; Shi, N.; Liu, Z. R.; Zhang, X. D.; Wu, M. Q.; Pan, C. F.; Liu, H. L.; Li, L. L.; Wang, Z. L. Transparent and Stretchable Triboelectric Nanogenerator for Self-Powered Tactile Sensing. *Nano Energy* **2019**, *59*, 302−310.

(35) Nie, J. H.; Chen, X. Y.; Wang, Z. L. Electrically Responsive Materials and Devices Directly Driven by the High Voltage of Triboelectric Nanogenerators. *Adv. Funct. Mater.* **2019**, *29*, 1806351.

(36) Ren, Z. W.; Nie, J. H.; Xu, L.; Jiang, T.; Chen, B. D.; Chen, X. Y.; Wang, Z. L. Directly Visualizing Tactile Perception and Ultrasensitive Tactile Sensors by Utilizing Body-Enhanced Induction of Ambient Electromagnetic Waves. *Adv. Funct. Mater.* **2018**, *28*, 1805277.

(37) Kwak, S. S.; Kim, S. M.; Ryu, H.; Kim, J.; Khan, U.; Yoon, H. J.; Jeong, Y. H.; Kim, S.-W. Butylated Melamine Formaldehyde as a Durable and Highly Positive Friction Layer for Stable, High Output Triboelectric Nanogenerators. *Energy Environ. Sci.* **2019**, *12*, 3156−3163.

(38) Nie, J.; Ren, Z.; Xu, L.; Lin, S.; Zhan, F.; Chen, X.; Wang, Z. L. Probing Contact-Electrification-Induced Electron and Ion Transfers at a Liquid-Solid Interface. *Adv. Mater.* **2020**, *32*, 1905696.

(39) Nie, J.; Wang, Z.; Ren, Z.; Li, S.; Chen, X.; Wang, Z. L. Power Generation from the Interaction of a Liquid Droplet and a Liquid Membrane. *Nat. Commun.* **2019**, *10*, 2264.

(40) Hinchet, R.; Yoon, H.-J.; Ryu, H.; Kim, M.-K.; Choi, E.-K.; Kim, D.-S.; Kim, S.-W. Transcutaneous Ultrasound Energy Harvesting Using Capacitive Triboelectric Technology. *Science* **2019**, *365*, 491−494.

(41) Choi, Y.; Yuen, C.; Maiti, S. N.; Olivares, S.; Gibbons, H.; Huls, H.; Raphael, R.; Killian, T. C.; Stark, D. J.; Lee, D. A.; Torikai, H.; Monticello, D.; Kelly, S. S.; Kebriaei, P.; Champlin, R. E.; Biswal, S. L.; Cooper, L. J. N. A High Throughput Microelectroporation Device to Introduce a Chimeric Antigen Receptor to Redirect the Specificity of Human T Cells. *Biomed. Microdevices* **2010**, *12*, 855−863.

I

(42) Guignet, E. G.; Meyer, T. Suspended-Drop Electroporation for High-Throughput Delivery of Biomolecules into Cells. *Nat. Methods* **2008**, *5*, 393−395.

(43) Boukany, P. E.; Morss, A.; Liao, W. C.; Henslee, B.; Jung, H. C.; Zhang, X. L.; Yu, B.; Wang, X. M.; Wu, Y.; Li, L.; Gao, K.; Hu, X.; Zhao, X.; Hemminger, O.; Lu, W.; Lafyatis, G. P.; Lee, L. J. Nanochannel Electroporation Delivers Precise Amounts of Bio-molecules into Living Cells. *Nat. Nanotechnol.* **2011**, *6*, 747−754.

(44) Bian, S. T.; Zhou, Y. C.; Hu, Y. W.; Cheng, J.; Chen, X. F.; Xu, Y. C.; Liu, P. High-Throughput *in Situ* Cell Electroporation Microsystem for Parallel Delivery of Single Guide RNAs into Mammalian Cells. *Sci. Rep.* **2017**, *7*, 42512.

(45) Li, Y.; Wu, M.; Zhao, D.; Wei, Z.; Zhong, W.; Wang, X.; Liang, Z.; Li, Z. Electroporation on Microchips: The Harmful Effects of pH Changes and Scaling Down. *Sci. Rep.* **2016**, *5*, 17817.

(46) Huang, H.; Wei, Z.; Huang, Y.; Zhao, D.; Zheng, L.; Cai, T.; Wu, M.; Wang, W.; Ding, X.; Zhou, Z.; Du, Q.; Li, Z.; Liang, Z. An Efficient and High-Throughput Electroporation Microchip Applicable for siRNA Delivery. *Lab Chip* **2011**, *11*, 163−172.

(47) McGinley, E. L.; Moran, G. P.; Fleming, G. J. P. Biocompatibility Effects of Indirect Exposure of Base-Metal Dental Casting Alloys to a Human-Derived Three-Dimensional Oral Mucosal Model. *J. Dent.* **2013**, *41*, 1091−1100.

(48) Ruzgys, P.; Novickij, V.; Novickij, J.; Satkauskas, S. Influence of the Electrode Material on ROS Generation and Electroporation Efficiency in Low and High Frequency Nanosecond Pulse Range. *Bioelectrochemistry* **2019**, *127*, 87−93.

(49) Wang, C.; Ding, Y.; Yuan, Y.; Cao, A.; He, X.; Peng, Q.; Li, Y. Multifunctional, Highly Flexible, Free-Standing 3D Polypyrrole Foam. *Small* **2016**, *12*, 4070−4076.

(50) Shen, G. H.; Hong, F. C. N. Ultraviolet Photosensors Fabricated with Ag Nanowires Coated with ZnO Nanoparticles. *Thin Solid Films* **2014**, *570*, 363−370.

(51) Chen, H. Y.; Gao, Y.; Zhang, H. R.; Liu, L. B.; Yu, H. C.; Tian, H. F.; Xie, S. S.; Li, J. Q. Transmission-Electron-Microscopy Study on Fivefold Twinned Silver Nanorods. *J. Phys. Chem. B* **2004**, *108*, 12038−12043.

(52) Garnett, E. C.; Cai, W.; Cha, J. J.; Mahmood, F.; Connor, S. T.; Greyson Christoforo, M.; Cui, Y.; McGehee, M. D.; Brongersma, M. L. Self-Limited Plasmonic Welding of Silver Nanowire Gunctions. *Nat. Mater.* **2012**, *11*, 241−249.

(53) Chen, H. J. A.; Hang, T.; Yang, C. D.; Liu, D.; Su, C.; Xiao, S.; Liu, C. L.; Lin, D. A.; Zhang, T.; Jin, Q. C.; Tao, J.; Wu, M.; Wang, J.; Xie, X. Functionalized Spiky Particles for Intracellular Biomolecular Delivery. *ACS Cent. Sci.* **2019**, *5*, 960−969.

(54) Ovcharenko, D.; Jarvis, R.; Hunicke-Smith, S.; Kelnar, K.; Brown, D. High-Throughput RNAi Screening *in Vitro*: From Cell Lines to Primary Cells. *RNA* **2005**, *11*, 985−993.

(55) Xu, Y. C.; Lu, Y.; Xing, W. L. An Individually Addressable Suspended-Drop Electroporation System for High-Throughput Cell Transfection. *Lab Chip* **2014**, *14*, 686−690.

(56) Moore, J. C.; Atze, K.; Yeung, P. L.; Toro-Ramos, A. J.; Camarillo, C.; Thompson, K.; Ricupero, C. L.; Brenneman, M. A.; Cohen, R. I.; Hart, R. P. Efficient, High-Throughput Transfection of Human Embryonic Stem Cells. *Stem Cell Res. Ther.* **2010**, *1*, 23.

(57) Zhan, Y. H.; Wang, J.; Bao, N.; Lu, C. Electroporation of Cells in Microfluidic Droplets. *Anal. Chem.* **2009**, *81*, 2027−2031.